Received: 5 September 2023 | Revised: 19 December 2023 | Accepted: 24 January 2024

DOI: 10.1002/mp.16984

RESEARCH ARTICLE

MEDICAL PHYSICS

An effective and robust lattice Boltzmann model guided by atlas for hippocampal subregions segmentation

Yingqian Liu[1,2,3] | **Min Wang**[2] | **Xianfeng Yu**[4] | **Ying Han**[4] | **Jiehui Jiang**[2] | **Zhuangzhi Yan**[1,2]

[1]School of Communication and Information Engineering, Shanghai University, Shanghai, China

[2]Institute of Biomedical Engineering, School of Life Sciences, Shanghai University, Shanghai, China

[3]School of Electrical Engineering, Shandong University of Aeronautics, Binzhou, China

[4]Department of Neurology, Xuanwu Hospital of Capital Medical University, Beijing, China

Correspondence
Jiehui Jiang, Institute of Biomedical Engineering, School of Life Sciences, Shanghai University, 99 Shangda Road, 200444, Shanghai, China.
Email: jiangjiehui@shu.edu.cn

Zhuangzhi Yan, Institute of Biomedical Engineering, School of Life Sciences, Shanghai University, 99 Shangda Road, 200444, Shanghai, China. Email: zzyan@shu.edu.cn

Yingqian Liu and Min Wang contributed equally to this study.

Funding information
National Natural Science Foundation of China, Grant/Award Numbers: 62376150, 62303295; Natural Science Foundation of Shandong Province, Grant/Award Number: ZR2015FL004

Abstract

Background: Given the varying vulnerability of the rostral and caudal regions of the hippocampus to neuropathology in the Alzheimer's disease (AD) continuum, accurately assessing structural changes in these subregions is crucial for early AD detection. The development of reliable and robust automatic segmentation methods for hippocampal subregions (HS) is of utmost importance.

Objective: Our aim is to propose and validate a HS segmentation model that is both training-free and highly generalizable. This method should exhibit comparable accuracy and efficiency to state-of-the-art techniques. The segmented HS can serve as a biomarker for studying the progression of AD.

Methods: We utilized the functional magnetic resonance imaging of the Brain's Integrated Registration and Segmentation Tool (FIRST) to segment the entire hippocampus. By intersecting the segmentation results with the Brainnetome (BN) atlas, we obtained coarse segmentation of the four HS regions. This coarse segmentation was then employed as a shape prior term in the lattice Boltzmann (LB) model, as well as for initializing contours. Additionally, image gradients and local gray levels were integrated into the external force terms of the LB model to refine the coarse segmentation results. We assessed the segmentation accuracy of the model using the Alzheimer's Disease Neuroimaging Initiative (ADNI) dataset and evaluated the potential of the segmentation results as AD biomarkers on both the ADNI and Xuanwu datasets.

Results: The median Dice similarity coefficients (DSC) for the left caudal, right caudal, left rostral, and right rostral hippocampus were 0.87, 0.88, 0.88, and 0.89, respectively. The proportion of segmentation results with a DSC exceeding 0.8 was 77%, 78%, 77%, and 94% for the respective regions. In terms of volume, the correlation coefficients between the segmentation results of the four HS regions and the gold standard were 0.95, 0.93, 0.96, and 0.96, respectively. Regarding asymmetry, the correlation coefficient between the segmentation result's right caudal minus left caudal and the corresponding gold standard was 0.91, while for right rostral minus left rostral, it was 0.93. Over time, we observed a decline in the volumes of the four HS regions and the total hippocampal volume of mild cognitive impairment (MCI) converters. Analysis of inter-group differences revealed that, except for the right rostral region in the ADNI dataset, the *p*-values for the four HS regions in the normal controls (NC), MCI, and AD groups from both datasets were all below 0.05. The right caudal hippocampal volume demonstrated correlation coefficients of 0.47 and 0.43 with the mini-mental state examination (MMSE) and Montreal cognitive assessment (MoCA), respectively. Similarly, the left rostral hippocampal volume showed correlation coefficients of 0.50 and 0.58 with MMSE and MoCA, respectively.

Conclusions: Our framework allows for direct application to different brain magnetic resonance (MR) datasets without the need for training. It eliminates the requirement for complex image preprocessing steps while achieving segmentation accuracy comparable to deep learning (DL) methods even with small sample sizes. Compared to traditional active contour models (ACM) and atlas-based methods, our approach exhibits significant speed advantages. The segmented HS regions hold promise as potential biomarkers for studying the progression of AD.

KEYWORDS
Alzheimer's disease, hippocampal subregions segmentation, lattice Boltzmann method

1 | INTRODUCTION

Alzheimer's disease (AD) is a neurodegenerative disease characterized by progressive cognitive decline. Effective diagnosis and treatment of AD are widely acknowledged as having substantial benefits for public health.[1] Previous research has indicated that structural magnetic resonance imaging (sMRI) holds promise as a noninvasive biomarker for assessing neurodegeneration in AD. Specially, hippocampal atrophy measurements from sMRI are commonly employed because they offer insights into early memory decline and can potentially indicate the progression from mild cognitive impairment (MCI) to AD.[2–5] Moreover, recent research has emphasized functional differences between the anterior and posterior axes of the hippocampus.[6] Given the variable sensitivity of distinct regions within the hippocampus to neuropathology in AD, scrutinizing structural alterations in hippocampal subregions (HS) can furnish more precise and sensitive information for the early detection of AD. Consequently, in the context of large cohorts, there is a pressing need to explore automatic, rapid, and accurate segmentation methods for HS. However, segmenting the hippocampus and its subregions presents particular challenges due to their small size and low contrast with surrounding tissues.

Manual hippocampal segmentation performed by radiologists is considered a gold standard, yet it is afflicted by drawbacks such as time intensiveness, high costs, and susceptibility to inter- and intra-rater variability. Various segmentation methods have proven successful for the entire hippocampus, encompassing traditional machine learning approaches,[7] atlas-based methods,[8] and active contour models (ACM).[9] Traditional machine learning approaches face limitations regarding the number of available training samples and the necessity for manual feature selection. Atlas methods, particularly multi-atlas methods, offer the advantage of facilitating segmentation in individuals with notable anatomical variability. Nevertheless, these methods entail multiple registration operations, thereby increasing their computational cost. ACM demonstrates effective utilization of anatomical prior information and image details, their drawback lies in the requirement to solve partial differential equations (PDE), which makes it unsuitable for processing large datasets. To promote research on automated HS segmentation, the Medical Segmentation Decathlon dataset provides 260 3D T1-weighted sMRI scans of the hippocampus along with corresponding ground truth of the rostral and caudal parts. Deep learning (DL) methods, including the 3D U-Net,[10] nnU-Net,[11] Nested Dilation Network (NDN),[12] have been applied to this dataset. While these methods achieve peak segmentation accuracy on this specific dataset, concerns arise regarding their robustness and generalizability due to the limited sample size. Furthermore, DL methods lack the utilization of anatomical priors, posing challenges in maintaining region consistency and achieving continuous segmentation.[13] The substantial hyperparameter search space and protracted training time further complicate the manual design of neural networks.[14]

The lattice Boltzmann (LB) method has found applications in various image processing tasks such as denoising, inpainting, registration and segmentation for its inherent parallelism and clear physical interpretation.[15–17] In the LB method, the fluid is discretized into particles distributed across nodes in a discrete space. During each time step, the particles within a node collide with each other and move to adjacent nodes until they reach an equilibrium state. A key feature is that the state of each node at the subsequent time step is determined exclusively by the states of its neighboring nodes, rendering it well-suited for parallel implementation. By considering the grayscale values of voxels in an image as the particle density in the fluid, and the redistribution of sub-voxels as the changes in grayscale values, the LB method can be effectively applied to 3D image processing. The collision and diffusion of sub-voxels is depicted as shown in Figure S1. In the context of image segmentation, an initial contour is established, conceptualized as an iso-density surface. The segmentation process subsequently evolves into a diffusion process of the contour within the medium, wherein conductivity varies, typically dictated by the image gradient.

Given the challenge of low contrast in the hippocampus and its subregions, it is difficult for the contour to accurately converge to the boundaries without a structural prior. To address this, we utilized the intersection of the Functional Magnetic Resonance Imaging of the Brain (FMRIB) Software Library (FSL)-Integrated Registration and Segmentation Tool (FIRST)[18] and the Brainnetome (BN) atlas[19] as a structural prior for the HS segmentation. The BN atlas provides masks for HS, but lacking a registration process between these masks and the target image leads to substantial segmentation errors. FSL FIRST provides segmentation of the entire hippocampus but still yields rough boundaries. By amalgamating the FSL FIRST results with the BN atlas, we achieve a more accurate determination of each subregion's location compared to using the BN atlas in isolation. This structural prior serves as an external force term in the LB fine segmentation model, furnishing initial contours for each subregion and expediting contour convergence towards boundaries. To enhance image segmentation precision, we introduced additional external force terms, including gradient term, penalty term, length term, and local intensity fitting term. The gradient term utilizes image gradients to guide the contour towards regions with substantial intensity variation. The penalty term penalizes contour deformations that deviate from desired smoothness. The length term encourages adherence to a desired contour length, and the local intensity fitting term enforces conformity to local intensity characteristics. Through the incorporation of these external force terms alongside the structural prior, our objective is to attain a more accurate and precise segmentation of the HS.

Our work encompasses several contributions, outlined as follows: (a) We propose a novel framework for the coarse localization and fine segmentation of HS. (b)The LB fine segmentation model employed in our work maximally leverages both anatomical prior information and information from the image to be segmented. The former ensures the structural integrity of segmentation, while the latter enhances the accuracy of the segmentation results. (c) We conducted comprehensive experiments on two distinct datasets: the Alzheimer's Disease Neuroimaging Initiative (ADNI) dataset and the Xuanwu dataset. By testing our framework on these different datasets, we validate its generality and adaptability across different imaging cohorts.

2 | METHODS

2.1 | System pipeline overview

Our HS segmentation framework follows a specific processing flow as shown in Figure 1. The processing flow can be summarized as follows: (1) Preprocessing: The image slated for segmentation and the BN atlas undergo registration to the Montreal Neurological Institute (MNI) standard space. This registration ensures proper alignment of both the image and atlas, facilitating accurate subsequent analyses. (2)Initialization: we employ the intersection of segmentation results derived from FSL-FIRST and the BN atlas as an initial, coarse segmentation of HS. This preliminary segmentation guides the determination of the initial contour for HS. (3) Segmentation model and external force construction: We first construct the LB segmentation model, and then combine various terms, including the length term, gradient term, penalty term, local intensity fitting term, and the shape term, to form the external force function of the LB model. (4) LB segmentation: The LB algorithm is executed using the external force function established in the preceding step. Further elaboration on each step within the framework will be provided in subsequent sections.

2.2 | Preprocessing

To begin with, each T1-weighted DICOM image was converted to the NIFTI format. Subsequently, both ADNI and Xuanwu subjects were normalized to the MNI standard T1 template (standard space $182 \times 218 \times 182$ with a resolution of $1\text{mm} \times 1\text{mm} \times 1\text{mm}$) through FSL's linear image registration tool (FLIRT). Following that, skull stripping was performed using FSL's brain extraction tool (BET). Once the skull stripping was completed, the resultant images were further normalized using FSL FLIRT. Furthermore, the BN atlas was resliced to fit the standard MNI space with a resolution of $1\text{mm} \times 1\text{mm} \times 1\text{mm}$, and subsequently, the caudal and rostral regions of the bilateral hippocampus were extracted as masks.

2.3 | Initialization

FSL FIRST performs a rough segmentation of the hippocampus, whereas the BN atlas divides each hippocampus into two sub-regions. By intersecting the segmentation results of FSL FIRST and BN atlas, a rough segmentation of HS was obtained for each subject. The result not only determines the initial contour of the HS, but also serves as a shape constraint term in the LB model.

2.4 | Segmentation model and external force construction

2.4.1 | Segmentation model

The LB evolution equation is defined as follows, the detailed explanation of this equation is provided in the Supplementary Material S01.

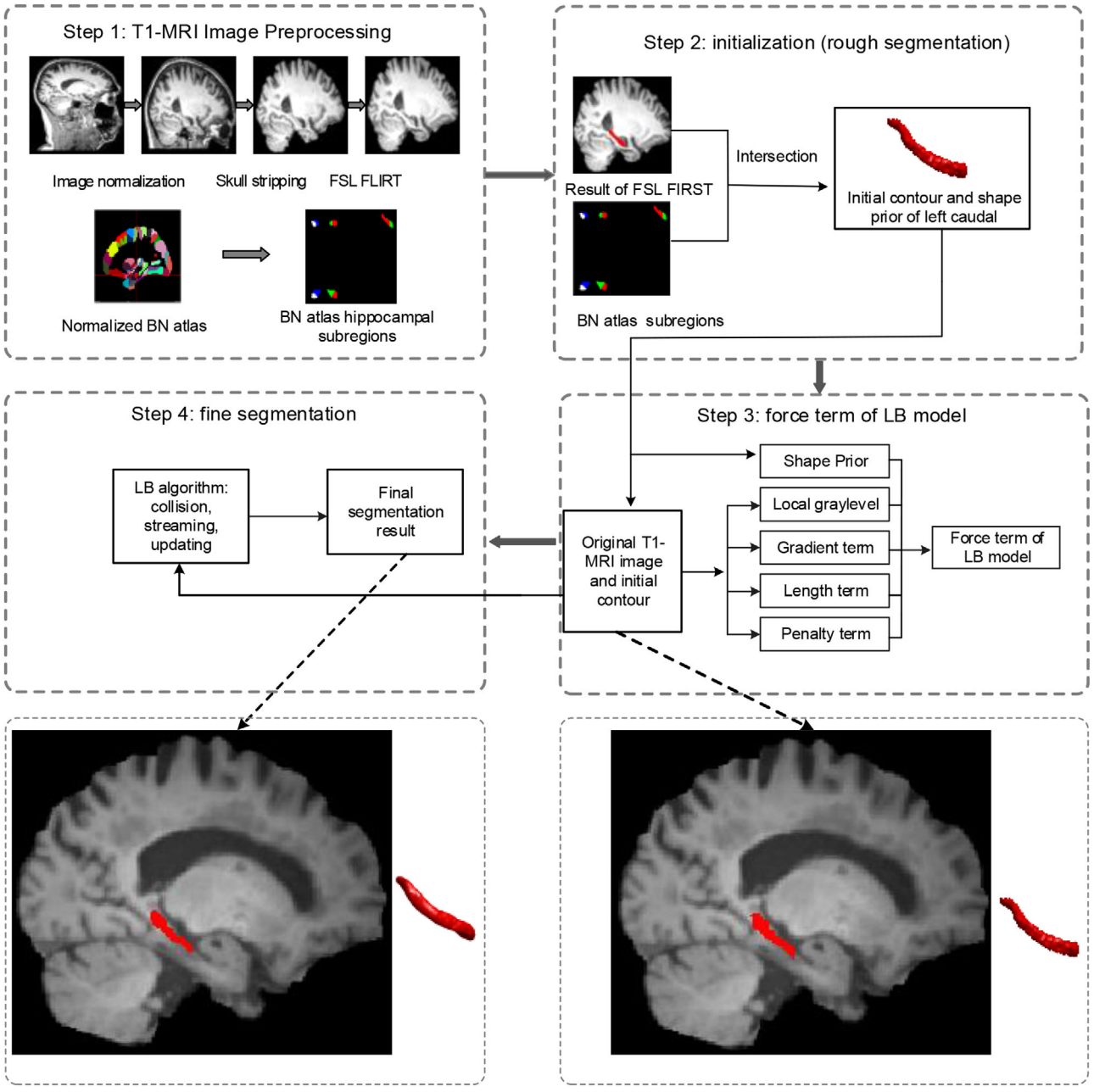

FIGURE 1 System pipeline of our HS segmentation framework. HS, hippocampal subregion.

$$I_\alpha(r + \mathbf{e}_\alpha \Delta t, t + \Delta t) - I_\alpha(r, t) = \frac{1}{\tau}\left[I_\alpha^{eq}(r, t) - I_\alpha(r, t)\right] + \Delta t \cdot F_\alpha, \tag{1}$$

By using Taylor expansion on the left side of Equation (1) and Chapmann-Enskog expansion on the right side of equation, we get:

$$\frac{\partial I}{\partial t} = \mathrm{div}(D\nabla I) + F \tag{2}$$

where, F is the external force term and D is the diffusion coefficient, where the image gradient is larger, the diffusion coefficient is smaller. We define $D = \frac{2}{1+20\cdot\nabla I} = \frac{1}{\tau}$, ∇ is gradient operator, so $\tau = 0.5 + 10 \cdot \nabla I$. Replacing I with level set ϕ, Equation (2) can be rewritten as:

$$\frac{\partial \phi}{\partial t} = \mathrm{div}(D\nabla \phi) + F \tag{3}$$

2.4.2 | External force term

To maximize the utilization of both structural prior and image information, the external force function incorporated into the LB model comprises four essential terms: the shape term, penalty term, length term, and local intensity fitting term.

The shape terms that provide strong constraints on contour evolution to prevent edge leakage are defined as follows,

$$S(\phi,\psi)=\int_{\Omega}(H(-\phi)-H(-\psi))^2dx \tag{4}$$

where

$$\psi(x,y)=\begin{cases}-c, & s(x,y)=1\\ c, & s(x,y)=0\end{cases} \tag{5}$$

s is the intersection of FSL FIRST and BN atlas, 1 represents the overlapping parts, 0 represents the no overlapping parts, c is a positive constant, H is the Heaviside function defined as follows:

$$H_{\varepsilon}(x)=\begin{cases}\frac{1}{2\varepsilon}\left[1+\frac{x}{\varepsilon}+\frac{1}{\pi}\sin\left(\frac{\pi x}{\varepsilon}\right)\right], & |\mathrm{x}|\le\varepsilon\\ 1, & \mathrm{x}>\varepsilon\\ 0, & \mathrm{x}<-\varepsilon\end{cases} \tag{6}$$

The penalty term constrains the degree to which the gradient of the edge deviates from 1. When the gradient of the edge can maintain 1, the corresponding zero level set is smooth and continuously differentiable everywhere.[20] The deviation is characterized by the following integral, where Ω represents the spatial domain of the image or the region of interest.

$$P(\phi)=\int_{\Omega}\frac{1}{2}(|\nabla\phi(x)|-1)^2dx \tag{7}$$

Length constraint, used to regularize the evolution curve C, ensuring that a sufficiently short curve is obtained. The length term is given by

$$L(\phi)=\int_{\Omega}\delta(\phi(x))|\nabla\phi(x)|dx \tag{8}$$

The local intensity fitting term uses kernel functions to extract intensity information from local regions to guide contour motion, enabling their models to handle intensity inhomogeneity.[21]

$$\begin{aligned}\varepsilon_{\mathrm{x}}^{LBF}(C,f_1(\mathrm{x}),f_2(\mathrm{x}))&=\lambda_1\int_{\mathrm{in}\,(C)}K(\mathrm{x}-\mathrm{y})|I(\mathrm{y})-f_1(\mathrm{x})|^2d\mathrm{y}\\&\quad+\lambda_2\int_{\mathrm{out}\,(C)}K(\mathrm{x}-\mathrm{y})|I(\mathrm{y})-f_2(\mathrm{x})|^2d\mathrm{y}\end{aligned} \tag{9}$$

where $K_{\sigma}(\mathrm{x})=\frac{1}{(2\pi)^{n/2}\sigma^n}e^{-|x|^2/2\sigma^2}$ is the kernel function, $\sigma>0$. $f_1(\mathrm{x})$ and $f_2(\mathrm{x})$ are two numbers that fit image intensities near the point x inside and outside contour. The kernel function assigns higher values to points y that are close to the center point x, gradually decreasing these values as the distance increases. Consequently, the image intensities at points y near x have a significant influence on determining the optimal values of f_1 and f_2, which minimize the energy function. The segmentation process focuses primarily on the image information surrounding the center point x, where the object of interest is expected to be situated.

The total energy function is

$$F_{\varepsilon}(\phi,f_1,f_2)=\beta\varepsilon_{\varepsilon}^{LBF}(\phi,f_1,f_2)+\mu P(\phi)+\nu L_{\varepsilon}(\phi)+\kappa S(\phi,\psi) \tag{10}$$

For a fixed level set function ϕ, the energy function $F_{\varepsilon}(\phi,f_1,f_2)$ is minimized with respect to the functions f_1 and f_2.

$$\begin{aligned}f_1(\mathrm{x})&=\frac{K_{\sigma}(\mathrm{x})*[H_{\varepsilon}(\phi(\mathrm{x}))I(\mathrm{x})]}{K_{\sigma}(\mathrm{x})*H_{\varepsilon}(\phi(\mathrm{x}))}\\ f_2(\mathrm{x})&=\frac{K_{\sigma}(\mathrm{x})*[(1-H_{\varepsilon}(\phi(\mathrm{x})))I(\mathrm{x})]}{K_{\sigma}(\mathrm{x})*[1-H_{\varepsilon}(\phi(\mathrm{x}))]}\end{aligned} \tag{11}$$

Keeping f_1 and f_2 fixed, and minimizing the energy functional $F_{\varepsilon}(\phi,f_1,f_2)$ with respect to ϕ, we derive the gradient descent flow:

$$\begin{aligned}\frac{\partial\phi}{\partial t}&=-\beta\delta_{\varepsilon}(\phi)(\lambda_1e_1-\lambda_2e_2)+\mu\left(\nabla^2\phi-\mathrm{div}\left(\frac{\nabla\phi}{|\nabla\phi|}\right)\right)\\&\quad+\nu\delta_{\varepsilon}(\phi)\,\mathrm{div}\left(\frac{\nabla\phi}{|\nabla\phi|}\right)+\kappa(\delta_{\varepsilon}(\phi)(H_{\varepsilon}(-\phi)-H_{\varepsilon}(-\psi)))\end{aligned} \tag{12}$$

where, δ is the Dirac delta function:

$$\delta_{\varepsilon}(\mathrm{x})=\begin{cases}\frac{1}{2\varepsilon}\left(1+\cos\left(\frac{\pi\mathrm{x}}{\varepsilon}\right)\right), & |\mathrm{x}|\le\varepsilon\\ 0, & |\mathrm{x}|>\varepsilon\end{cases} \tag{13}$$

$$e_1(x) = \int_\Omega K_\sigma(y-x)|I(x) - f_1(y)|^2 dy$$
$$e_2(x) = \int_\Omega K_\sigma(y-x)|I(x) - f_2(x)|^2 dy \quad (14)$$

The external force function for LB evolution equation is defined as the right side of Equation (12).

2.5 | LB segmentation

After the initial contour, external force function and relaxation factor are determined, the following LB algorithm can be used to complete the segmentation of the HS (Algorithm 1).

ALGORITHM 1 LB algorithm for HS segmentation

1. Setting the position of evolving curve C according to preprocessing and initialization steps and defining level set function ϕ as a signed distance function, such as: $\phi(r,0) = \begin{cases} -c, r \in C_{in} \\ 0, \quad r \in C \\ c, r \in C_{out} \end{cases}$ where r is the position of one voxel in image, $c > 0$ is a constant, C_{in} and C_{out} denote the inside and outside region of evolving curve C respectively.
2. Initialize local equilibrium distribution function $\phi_\alpha^{eq}(r,0) = \omega_\alpha \phi(r,0)$, compute relaxation parameter τ.
3. Compute the external force term with Equation (12).
4. Updating the evolving curve and $\phi(r,t) = \sum_\alpha \phi_\alpha^{eq}(r,t)$ after evolution with Equation (1).
5. If the segmentation is not done, jump to step (2).
6. Output the segmentation result.

3 | EXPERIMENTS

3.1 | Data

We have curated two distinct datasets, namely ADNI and Xuanwu. The demographic and clinical information is summarized in Table 1, additional details about the the image acquisition are provided in Table S1, the inclusion and exclusion criteria for Xuanwu data can be found in Supplementary Material S02 (Xuanwu data). AD subjects in ADNI database are $A\beta$ positive, the NC subjects are $A\beta$ negative. The subjects in Xuanwu are all Chinese, and the 38 MCI patients listed are all MCI convertors aged from 50 to 88, the data listed are baseline data. All MCI convertors have undergone at least two MRI and clinical examinations.

3.2 | Subjective segmentation quality assessment

To visually show the segmentation efficacy of our methodology, we initially selected a subset of segmentation results for representation. Additionally, we conducted ablation experiments to assess the impact of specific components, with particular emphasis on the absence of shape priors and local intensity fitting terms in our approach. Our objective is to elucidate the individual contributions of these components to the overarching segmentation performance. Furthermore, we present segmentation outcomes for diverse initial contours under consistent external force terms, iteration steps, and parameters, thereby validating the effectiveness of our proposed method in initial contour determination. Moreover, we showcased hippocampal segmentation performances of two classical ACMs, namely, distance regularized level set(DRLS)[22] and Chan-Vese model. Finally, we solicited feedback from two experts affiliated with Xuanwu Hospital, who critically evaluated the aforementioned segmentation results.

3.3 | Objective segmentation quality assessment

3.3.1 | Dice similarity coefficients distribution

Two seasoned neurosurgery experts meticulously performed gold-standard manual segmentations for 121 MCI subjects from the ADNI dataset. Each subject's hippocampus was manually segmented to four HS. The Dice similarity coefficients (DSC) were calculated for the four HS, serving as a metric to quantify their similarity with ground truth. In examining the spatial extent of the segmentations, we analyzed the histogram distribution of the DSC values for the four HS which provide insights into the mean, variance, maximum, and minimum DSC values. To evaluate the effectiveness of our proposed method, we compared it with the BNLB approach which solely relies on a BN atlas as the shape prior and employs the LB model for refinement.

3.3.2 | Subregion volume correlation analysis

Unlike overlapping metrics such as DSC, the volume of segmentation results is considered to be less sensitive to resolution and boundary effects. In this section, our analysis centered on examining the Pearson correlation[23] between the volumes of the four HS in 121 subjects from the ADNI dataset and their corresponding manual segmentations. A strong correlation

TABLE 1 Demographic information of ADNI and Xuanwu subjects.

		NC	MCI	AD	Inferential statistics
ADNI	Sample Size	96	121	64	
	Gender (M/F)	47/49	69/52	41/23	$\chi^2 = 3.67, P = 0.16$
	Age	74.2 ± 6.5	72.6 ± 7.6	74.0 ± 8.7	$F = 1.369, P = 0.256$
	MMSE	29.2 ± 1.0	26.4 ± 3.8	22.8 ± 2.2	$F = 3202.3, P \leq 0.01$
Xuanwu Hosptial	Sample Size	73	38	55	
	Gender (M/F)	33/40	21/17	18/37	$\chi^2 = 4.825, P = 0.09$
	Age	65 ± 5.4	70.9 ± 9.3	70.9 ± 9.1	$F = 10.8, P \leq 0.001$
	MMSE	28.8 ± 1.3	23.3 ± 3.9	16.1 ± 5.6	$F = 4603.1, P \leq 0.01$

Note: Demographic and clinical data are compared using a one-way ANOVA, and the gender data are analyzed by a χ^2 test.
Abbreviations: AD, Alzheimer's disease; ADNI, Alzheimer's Disease Neuroimaging Initiative; ANOVA, analysis of variance; MCI, mild cognitive impairment; MMSE, Mini-Mental State Examination; NC, normal controls.

suggests that the segmentation results hold promise for longitudinal analyses of disease progression.

3.3.3 | Subregion volume asymmetry correlation analysis

Building upon previous research highlighting the presence of asymmetry between the left and right hippocampal structures, our exploration involved calculating the difference between the volumes of the right subregion and the left subregion for each participant. Subsequently, we performed a Pearson correlation analysis to assess the degree of agreement between these asymmetry values obtained through our method and the corresponding gold standard measurements.

3.3.4 | Comparison with state of art

To benchmark our method against DL-based approaches, we implemented three methods that have been applied to HS segmentation, including NDN, nnU Net, and 3D Unet, and one DL method for hippocampal segmentation, HGM-cNet.[24] The first three DL methods were configured based on established processing flows reported in the literature. To assess their performance, we conducted five-fold cross-validation on a dataset comprising 120 subjects from the MCI group in ADNI. The intersection of HGM-cNet and BN atlas is used as the segmentation result for HS. For a comprehensive comparison, we applied two traditional methods, multi-atlas and ACM to our dataset. The multi-atlas method employed fast 'coarse-fine' registration to mitigate computational costs, and the HS were obtained through the intersection of its segmentations with BN atlas. The ACM method utilized in our study is the DRLS, where the segmentation process mirrored our framework, and the external force term of ACM resembled our LB model. The evaluation metric used was DSC and its standard deviation (SD). Additionally, we compared the segmentation speeds of atlas-based methods, ACM, and our proposed method. To underscore certain limitations of DL methods, such as hole and boundary discontinuity issues due to insufficient samples and the absence of anatomical priors, we presented the segmentation results of two DL models: a convolutional neural network (CNN)[25] model trained with 25 000 hippocampus samples and the Segment Anything model.[26]

3.4 | Clinical application potential research

To establish the clinical significance of our method, three experiments were conducted. First, we investigated changes in HS volume over time in four MCI converters from Xuanwu. Second, we employed the analysis of variance (ANOVA) method to scrutinize volume differences among the NC, MCI, and AD groups for all four HS in the two datasets. This analysis aimed to assess the statistical discriminatory capabilities of HS volume in distinguishing between these clinical groups. Finally, a random selection of 123 subjects from the ADNI and Xuanwu datasets was made to explore the correlation between HS volume and clinical outcomes, such as MMSE and MoCA scores. This analysis aimed to determine whether a significant correlation existed between subregion volumes and cognitive performance.

3.5 | Implementation

The experimental hardware platform is Intel (R) Core (TM) i7-9750H CPU @ 2.60GHz, 8 GB memory, one NVIDIA GeForce GTX 1650 graphics card. We have installed win10 and Ubuntu on this computer. FSL is installed on Ubuntu system, Matlab is installed on win10 system. The number of iterations for segmenting each HS is set to 4. The remaining parameters are $\lambda_1 = \lambda_2 = 1, \beta = 1/15, \kappa = 50, \mu = 0.01, \nu = 2, \varepsilon = 0.5$.

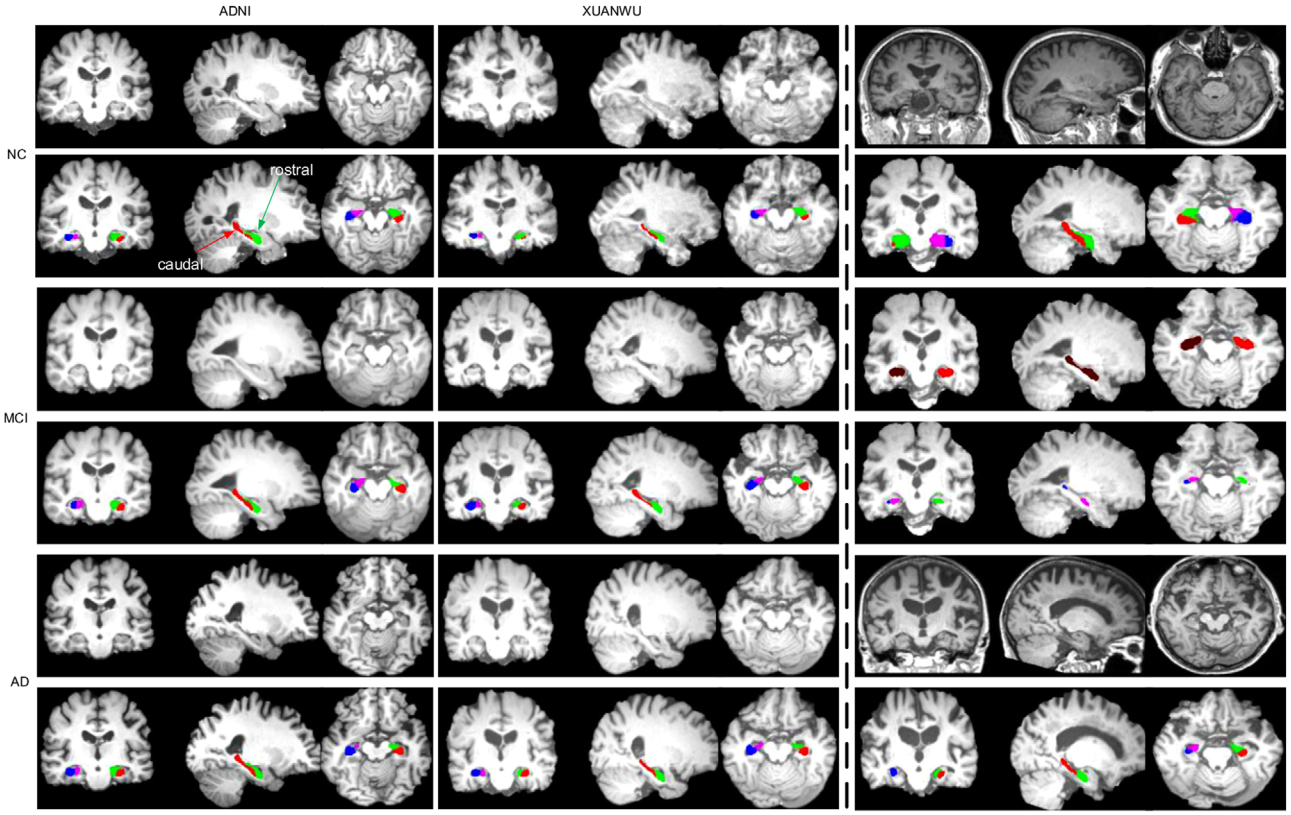

FIGURE 2 Left column is three subjects from ADNI, middle column is three subjects from Xuanwu dataset. From top to bottom, NC subjects, MCI subjects and AD subjects are in order. The first four rows of the right column display images with residual necks, BN atlas segmentation, FSL segmentation, and our method's result, respectively. The last two lines display the tilted head image and the segmentation results of our method. AD, Alzheimer's disease; ADNI, Alzheimer's Disease Neuroimaging Initiative; BN, brainnetome; FSL, Functional Software Library; MCI, mild cognitive impairment; NC, normal controls.

4 | RESULTS

4.1 | Subjective segmentation quality evaluation

Figure 2 showcases HS segmentation results for eight subjects. The left column features three subjects from the ADNI, while the middle column displays three subjects from the Xuanwu. These segmentation outcomes serve as compelling evidence of the efficacy of our method in accurately delineating the HS across diverse subjects, including both healthy controls and individuals with neurological conditions. The demonstrated performance across different datasets underscores the robustness and reliability of our method. The right column illustrates two undesirable scenes in the image preprocessing and imaging stages, neck residue and head tilt. The first four lines respectively display the images with residual neck, BN atlas segmentation results, FSL segmentation results, and the segmentation results of our method. The last two lines show the tilted head image and the segmentation results of the proposed method. Following a meticulous examination of all segmentation results, both experts concurred that our method performs effectively in head-moving images. However, in instances where severe neck residue is present after image preprocessing, our method may encounter challenges in accurately segmenting the caudal hippocampus due to deviations in the BN atlas.

Figure 3 illustrates the results of an ablation experiment and the segmentation results of two classic ACMs. Panels (a), (b), and (c) showcase the segmentation outcomes when the shape prior term is not considered, with corresponding values of the local intensity fitting term parameter β set at 0.2, 0.07, and 0.01, respectively. As the β parameter increases, the model becomes more sensitive to edges. Panels (d), (e), and (f) display the segmentation results without the local intensity fitting term but with the shape term, using iteration numbers of 4, 8, and 10. Meanwhile, panels (g), (h), and (i) present the segmentation results when both the shape term and local intensity fitting term are utilized, again with iteration numbers of 4, 8, and 10. Notably, the shape prior term ensures that the contour closely aligns with the hippocampus's edge. However, in the absence of the local intensity fitting term, the contour's topological deformability appears to be limited. Further investigation reveals that using a cube near the hippocampus as the initial

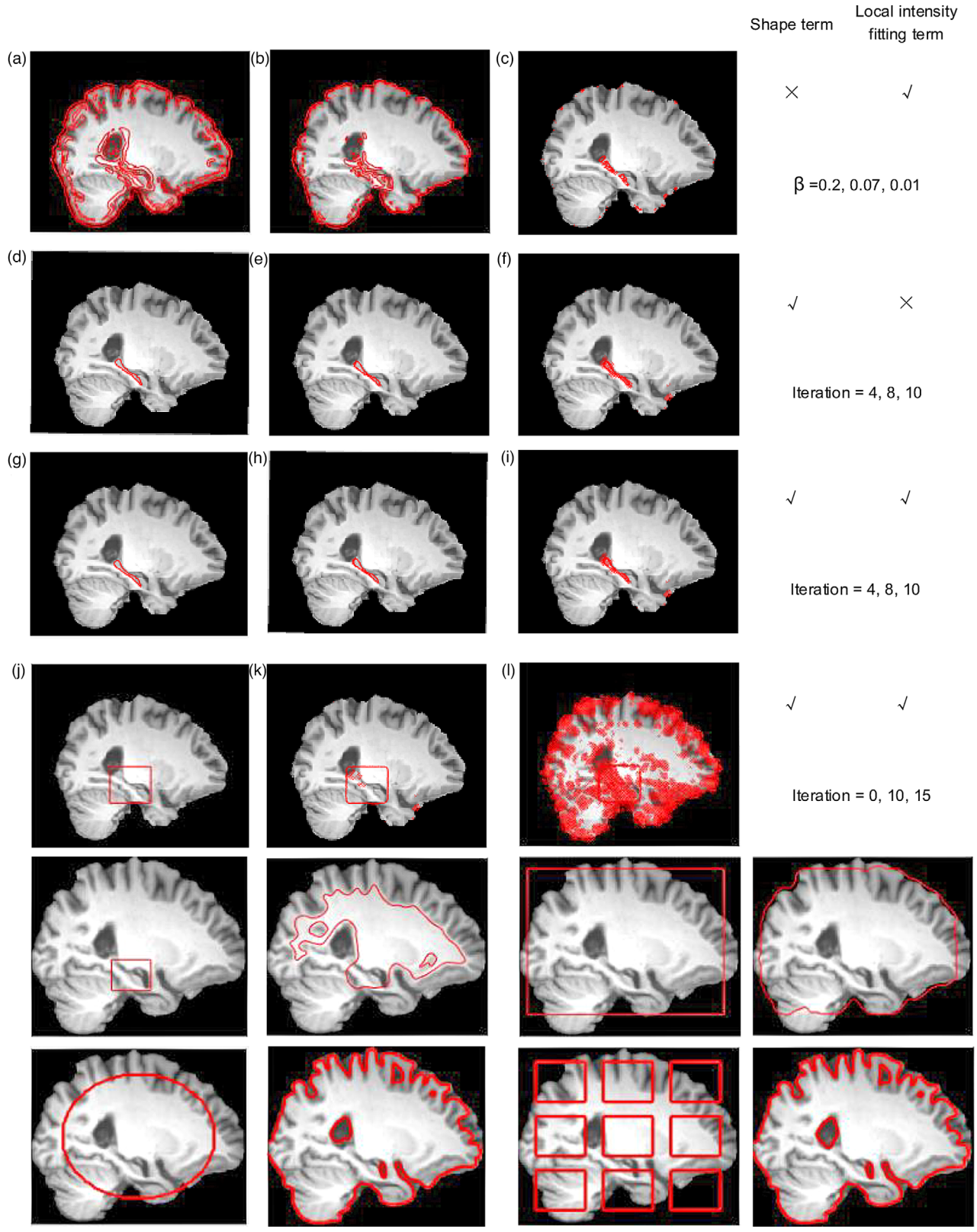

FIGURE 3 Results of ablation experiments and comparison with classical ACM. (a), (b), (c) shows the segmentation results without shape prior term, the local binary fitting term parameter are equal to 0.2, 0.07, and 0.01. (d), (e), (f) shows the segmentation results without local binary fitting term, the iteration number is 4, 8, 10. (g), (h), (i) shows the segmentation results with shape term and local binary fitting term, the iteration number is 4, 8, 10. (j), (k), and (l) shows the segmentation results using a cube as the initial contour, with iterations of 4, 8, and 10. The penultimate row illustrates the segmentation outcomes of DRLS under distinct initial contours, while the final row delineates the segmentation performance of the Chan-Vese model under varying initial contour lines. ACM, active contour models; DRLS, distance regularized level set.

contour fails to achieve accurate segmentation, affirming the necessity of our method for determining the initial contour. We discovered that classical ACMs, particularly the Chan-Vese model, are unable to successfully accomplish hippocampal segmentation. This limitation arises from the model's emphasis on global intensity rather than local intensity, rendering it less effective in capturing the nuanced features essential for accurate segmentation in this specific context.

4.2 | Objective segmentation quality assessment

4.2.1 | DSC distribution

The DSC distribution map of all 121 MCI subjects in ADNI can be found in Supplementary Material S03 Figure S2. Specifically: For the left caudal hippocampus, the BNLB method's mode is located at 0.61, and the DSC of all subjects is below 0.8. In contrast, our method's mode is positioned at 0.87, with over 77% of subjects achieving a DSC greater than 0.8. Similarly, for the right caudal hippocampus, the BNLB method's mode is at 0.58, and all subjects' DSC values are below 0.8. Our method's mode is at 0.88, with over 78% of subjects surpassing a DSC of 0.8. Regarding the left rostral hippocampus, the BNLB method's mode is located at 0.55, and the DSC values of all subjects are below 0.8. Conversely, our method's mode is at 0.88, with over 77% of subjects achieving a DSC greater than 0.8. For the right rostral hippocampus, the BNLB method's mode is at 0.64, with only five subjects having a DSC greater than 0.8. In contrast, our method's mode is at 0.89, with the majority (94%) of subjects surpassing a DSC of 0.8. The experimental results demonstrate the superiority of our method over BNLB in terms of accuracy and stability, underscoring the significant advantages of our approach in coarse localization compared to BN atlas.

4.2.2 | HS volume correlation analysis

Figure 4 presents a scatter plot depicting the correlation between our method's results and the gold standard for four HS. Notably, a clear correlation is observed, albeit with a few outliers. Specifically, the correlations for each subfield are as follows: 0.95 for the left caudal, 0.93 for the right caudal, and 0.96 for both the left and right rostral regions. A linear regression line is included on the plot, with slope values of 1.03, 1.01, 1.11, and 1.09 for the respective regions. The last row of Figure 4 displays the difference in volume between the right and left hippocampi, as determined by our method and the ground truth, across all MCI subjects in ADNI. By excluding outliers, a correlation coefficient of 0.91 is achieved for the caudal hippocampus, while a correlation coefficient of 0.93 is attained for the rostral hippocampus. These two experiments collectively demonstrate that our method can achieve segmentation accuracy comparable to that of the gold standard.

4.2.3 | Comparison with state of art

Table 2 provides an overview of the segmentation accuracy for various methods, including DL methods, muti-atlas method, BN-atlas method, ACM method, and our method. Our method ranks third in DSC scores for both the caudal and rostral hippocampus, while HGM-cNet achives the highest segmentation accuracy due to the addition of hippocampal gray matter probability maps. However, it is crucial to acknowledge that, due to the limited sample size of our data, nnU-Net, NDN and 3D-Unet do not demonstrate significant advantages in segmentation accuracy. In contrast to other methods, the BN atlas exhibits the lowest segmentation accuracy, primarily attributed to its exclusion of the registration process for the segmented image. Notably, the ACM method, employing identical processing flow and external force functions as our approach, achieves comparable accuracy levels to our method. The SD of the DSC values serves as an indicator of variability in segmentation accuracy, with a smaller SD reflecting a more stable method. Notably, the muti-atlas method exhibits the smallest SD, signifying superior stability. While our method's SD is greater than that of the atlas method, it remains smaller than nnU-Net, NDN and 3D-Unet. The SD of our method's DSC primarily arises from the image preprocessing stage and initialization process. Conversely, for DL methods, the reason could be insufficient features caused by the limited amount of data.

Figure 5 illustrates certain limitations associated with DL methodologies in the context of hippocampal segmentation. While the CNN model, trained with an extensive dataset of 25 000 samples, demonstrated commendable accuracy and speed, it exhibited discontinuities in the segmented boundaries, as indicated by the arrows in the first row and second column. The Segment Anything model, designed as a universal approach, faced notable challenges in accurately segmenting the hippocampus. Despite providing an initial contour, the automatic segmentation results displayed a substantial error. Although interactive operation led to improved segmentation accuracy, a significant disparity with the gold standard remained.

We conducted a thorough analysis of speed performance across different segmentation methods. The multi-atlas method emerged as the most time-consuming, requiring approximately 270 s for the segmentation of a unilateral hippocampus. The ACM model exhibited a faster performance, taking around 80 s for segmenting a subregion of the unilateral

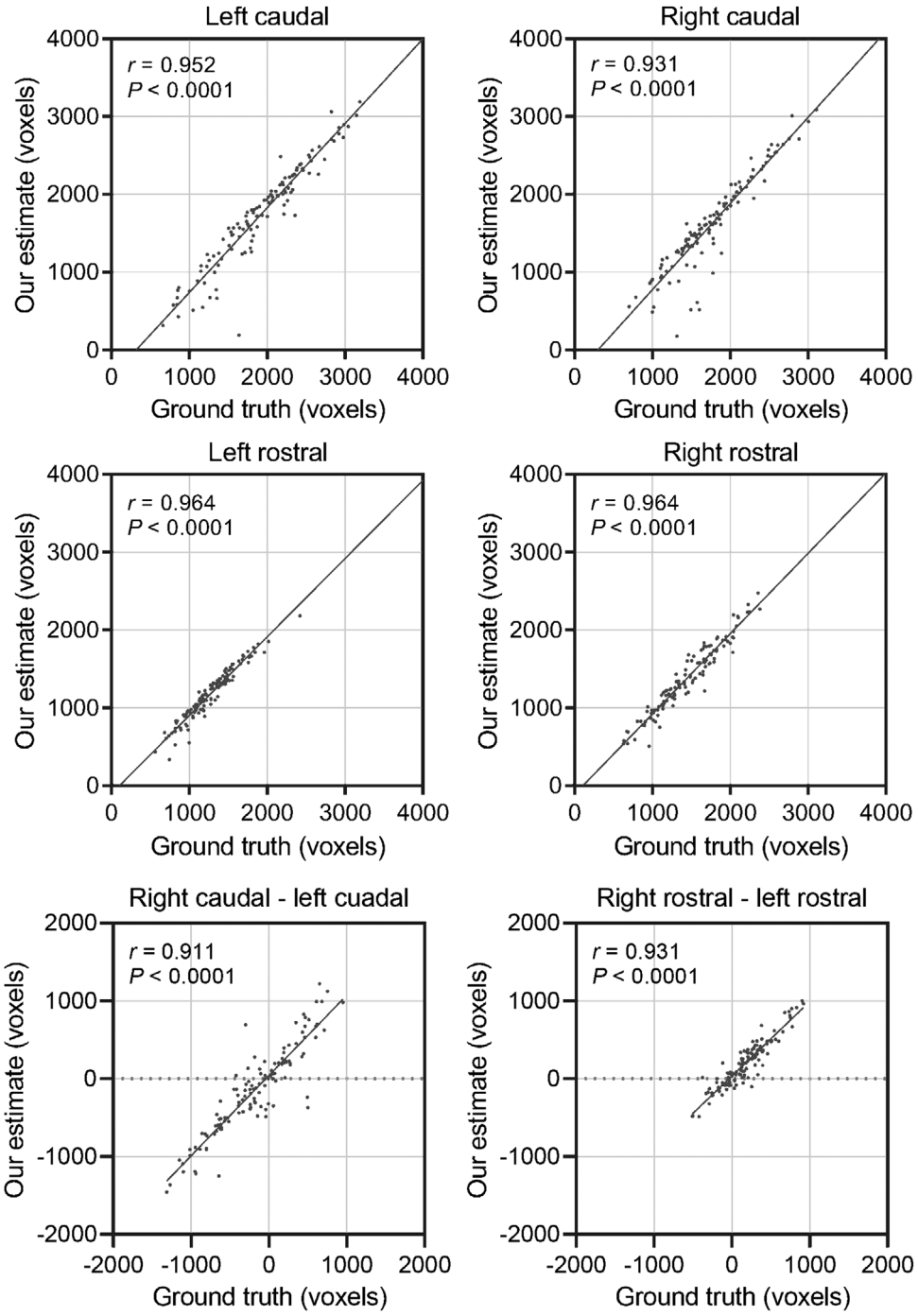

FIGURE 4 Comparison of the estimated HS volume with ground truth (first two rows) and distribution of hippocampal volume a symmetries (last row). HS, hippocampal subregion.

hippocampus. In contrast, our method demonstrated remarkable efficiency, completing the segmentation task in approximately 10 s. The major portion of the total segmentation time was attributed to image initialization, specifically the FSL FIRST segmentation, which took roughly two and a half minutes. Factoring in the initialization time, the ACM method took approximately 470 s for the sequential segmentation of four HS, with a parallel time of approximately 230 s. In comparison, our method achieved a sequential segmentation time of around 190 s and a parallel segmentation time of approximately 160 s. It is noteworthy that we did not analyze the segmentation speed of DL methods in this context, as their time consumption is primarily associated with data preprocessing and model training stages.

TABLE 2 Comparison with state of art.

Method		Time (s)			DSC [%] Rostral	DSC [%] Caudal
DL	nnU-Net	–			85.6 ± 0.059	85.2 ± 0.063
	NDN	–			83.9 ± 0.051	84.3 ± 0.064
	3D-Unet	–			83.5 ± 0.062	82.5 ± 0.063
	HGM-cNet	–			88.8 ± 0.045	88.6 ± 0.044
Muti-atlas	fast "coarse-fine" registration	270 s			84.2 ± 0.016	84.1 ± 0.017
BN-atlas					80.5 ± 0.060	80.9 ± 0.058
		FSL	**Serial**	**Parallel**		
ACM		150 s	320 s	80 s	84.1 ± 0.055	82.2 ± 0.080
Our method		150 s	40 s	10 s	85.0 ± 0.049	84.3 ± 0.062

Abbreviations: ACM, active contour models; BN, brainnetome; DL, deep learning; DSC, dice similarity coefficients; FSL, Functional Software Library; NDN, Nested Dilation Network.

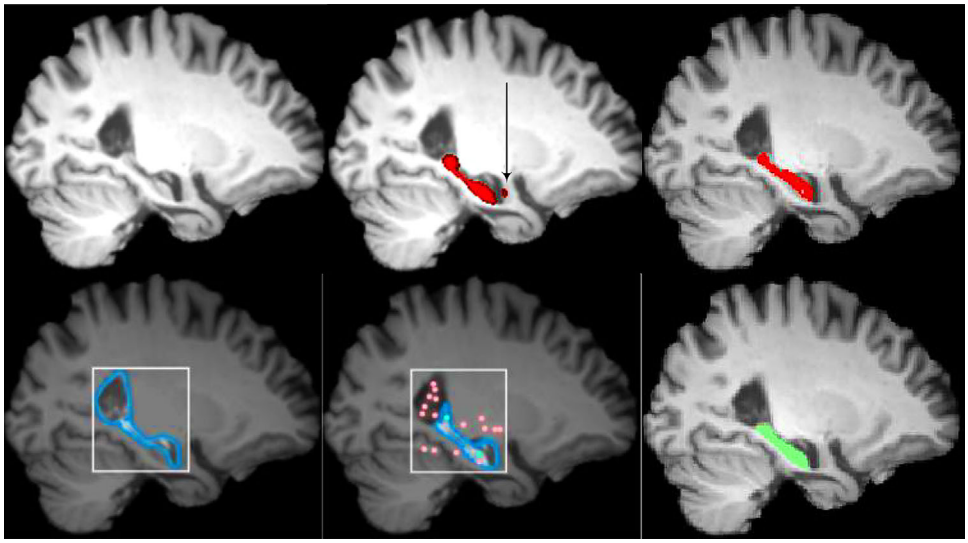

FIGURE 5 Subjective comparison between our method and DL methods. From left to right, top to bottom, the six images are the original image, CNN segmentation result, our result, coarse segmentation and interactive segmentation result of the Segment Anything model, and the gold standard. CNN, convolutional neural network; DL, deep learning.

4.3 | Clinical application potential research

Figure 6 depicts a noticeable trend indicating a decrease in volume for the hippocampus and its subregions, implying that our method effectively detects longitudinal changes in the hippocampus. Table 3 provides a comprehensive summary of group differences among individuals classified as NC, MCI, and AD. In the ADNI dataset, significant differences were observed in the right caudal, left rostral, and right rostral subregions. In the Xuanwu dataset, significant differences were found in all four subregions. Intriguingly, for both the ADNI and Xuanwu datasets, the left rostral volume emerges as more effective in distinguishing between NC, MCI, and AD groups. In the analysis involving 123 subjects, Pearson correlation coefficients revealed specific associations: the right caudal hippocampus exhibited a correlation of 0.47 with MMSE and 0.43 with MoCA, while the left rostral hippocampus demonstrated a correlation of 0.50 with MMSE and 0.58 with MoCA. However, the correlation between the left caudal and right rostral volumes with MMSE and MoCA was found to be weak. These results suggest that the right caudal and left rostral volumes may serve as more indicative measures of cognitive function, as assessed by MMSE and MoCA scores. However, the left caudal volume and right rostral volume appear to have less pronounced associations with cognitive performance in this analysis.

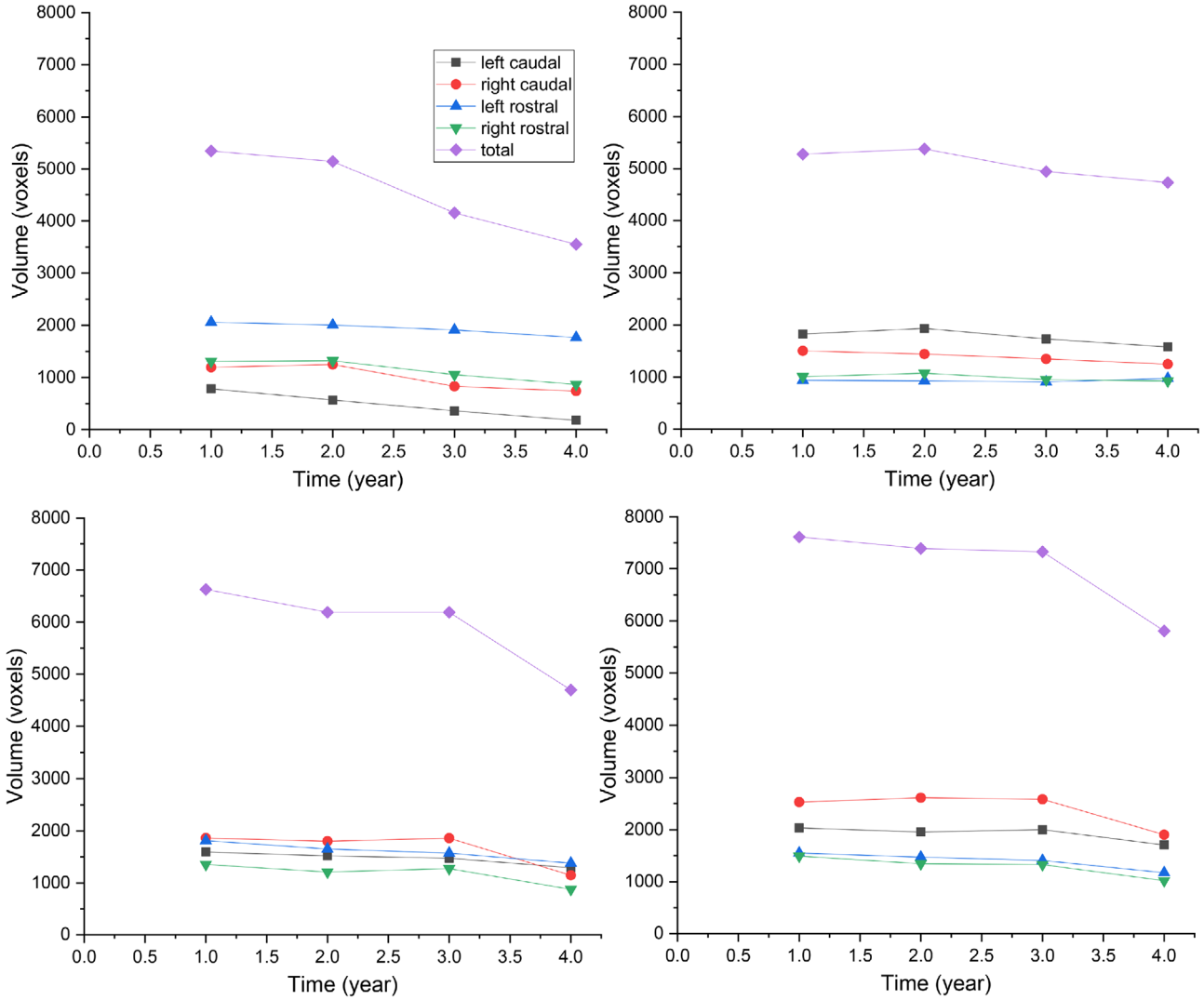

FIGURE 6 Hippocampal volume estimate versus time, using our methods on four subjects in Xuanwu. Four subregions volume and total volume are plotted.

TABLE 3 Inter-group differences.

		Inferential statistics			
	Groups	Left caudal	Right caudal	Left rostral	Right rostral
ADNI	NC	$F = 3.042$	$F = 18.350$	$F = 39.471$	$F = 0.366$
	MCI	$P = 0.049$	$P \leq 0.05$	$P \leq 0.05$	$P = 0.694$
	AD				
xuanwu	NC	$F = 9.740$	$F = 19.417$	$F = 57.567$	$F = 15.030$
	MCIc	$P \leq 0.05$	$P \leq 0.05$	$P \leq 0.05$	$P \leq 0.05$
	AD				

Note: MCIc represents MCI converter.
Abbreviations: AD, Alzheimer's disease; ADNI, Alzheimer's Disease Neuroimaging Initiative; MCI, mild cognitive impairment; NC, normal controls.

5 | DISCUSSIONS

We developed an automatic HS segmentation framework that offers several advantages. First, our methods segmentation accuracy remains robust across different brain MRI datasets, independent of the training sample size. This adaptability allows for effective application to diverse datasets without the need for extensive training.

Second, our method showcases superior segmentation speed when compared to ACM and atlas-based methods. A distinctive feature of this approach is the close proximity of the automatically determined initial contour to the target segmentation area. In cases of minor deviation, the resulting segmentation error arising from the initial contour's positioning remains within acceptable parameters. Conversely, when the initial contour is positioned at a considerable distance from the intended hippocampal segmentation region as we manually drawn, achieving precise segmentation outcomes becomes unattainable. This experiment substantiates the effectiveness of the initial contour determined by our methodology in facilitating accurate segmentation. Moreover, the segmentation results generated by our method exhibit smoothness and continuity, ensuring high-quality outputs. Preliminary experiments indicated that the HS volumes obtained through our method hold clinical application potential.

Segmenting the hippocampus poses challenges due to low contrast with surrounding tissues and the deformation it undergoes with age or disease progression. Traditional segmentation models relying solely on image information or strong priors struggle to succeed in this task. In contrast, our method leverages both prior anatomical structure information and image-specific details. The former is derived from the intersection of FSL-based coarse segmentation and BN atlas, while the latter incorporates local grayscale, gradient, and another image information. By introducing a shape prior, our method addresses the boundary leakage issue encountered by traditional LB models when segmenting the weakly bounded hippocampus. Initializing the contour using the edge of the prior shape serves two purposes: determining the approximate location of the hippocampus subregion and expediting the convergence of the initial contour. For the rostral and caudal hippocampus, our method achieves a DSC of 85.0 $\pm$ 0.049 and 84.3 $\pm$ 0.062, respectively. According to the literature, the DSC of the rostral and caudal hippocampus of NDN network is 87.9 and 88.7 respectively; SS-3DCAPSNET[27] is 81.6, 80.0; nnU-Net is 89.9, 88.2; DDI-Net[28] is 92, 89. The mean DSC of dilated deeply supervised network[29] is 88.2. Comparing our results to those reported in the literature, we rank fifth and may appear at a disadvantage. It is important to note that the cited literature's results are based on their own datasets. Our experimental findings confirm that when the training sample size is small (our dataset's size is smaller than the Medical Segmentation Decathlon dataset), DL methods do not hold an advantage as they struggle to extract sufficient features. In contrast, our method does not require training and is not affected by the size of the training data, enhancing its generalizability. Compared to Atlas methods and DL approaches, our method yields smooth and continuous edges, eliminating the need for post-processing steps such as denoising. This feature facilitates subsequent morphological analysis, offering convenience and efficiency.

Compared to traditional ACM and Atlas methods, the LB algorithm offers significant speed advantages due to its inherent parallelism and simple code. The former is limited by the solution of PDE, while the latter is constrained by complex registration and label fusion processes. In terms of speed, our framework does not have an advantage over trained DL model. For example, it takes about 10 s for a trained CNN model to segment bilateral hippocampus on our platform.[25] However, DL methods often entail longer image preprocessing and training times. For instance, to reduce resource consumption, DL models for hippocampus segmentation are often trained on a subset of the brain image that focuses only on the region of interest, which involves time-consuming region extraction steps. In contrast, our segmentation is directly performed on standardized and skull-removed brain images, eliminating the need for region extraction.

Indeed, our method can be considered as a refined segmentation approach that leverages both coarse segmentation and fine segmentation steps. The coarse segmentation utilizes FSL and BN atlas, while the fine segmentation uses an LB model. The choice of using FSL FIRST and the BN atlas in our method is based on their successful applications in brain science.[30–32] Moreover, the LB model, which is a widely adopted technique in image segmentation, is employed in our fine segmentation step. It is worth mentioning that our framework is not limited to hippocampal segmentation alone. It can be applied to fine segmentation of other brain tissues in MRI images. By adapting the coarse segmentation step and incorporating relevant structural priors, our method can be extended to segment various brain structures.

Our method has certain limitations. The experimental results suggest that the precision of segmentation is compromised in cases where prior information is either absent or unreliable. Nevertheless, the physicians at Xuanwu Hospital posit that the inherent bias within our proposed method remains confined within an acceptable threshold. They have recognized our work, expressed interest in implementing our method within clinical practice, and committed to the ongoing provision of new data and annotations to substantiate the validity of our approach. We only studied the relationship between clinical evaluation and HS volume. However, studying the relationship between changes in clinical evaluation and changes in HS volume can provide more insights into the clinical effectiveness of our method. In addition, our method mainly considers the volume of HS rather than its morphology, which is a more sensitive biomarker.[33] In the next step of clinical application research, after extending the dataset, we will use radiomics to extract features of HS,[34] and then conduct two studies: (1) to study the effectiveness of these features with HS volume in NC, MCI, and AD

classification; (2) to investigate the biological basis of these features, that is their correlation with biomarkers such as Aβ and Tau. In summary, improving the accuracy of our method and exploring its clinical application potential are our next research directions.

6 | CONCLUSIONS

We propose a robust framework for HS segmentation. The segmentation accuracy and speed of this method are comparable to state of art methods, and it has good generality. Clinical analysis shows that the HS obtained by this method can serve as potential biomarkers for studying the progression of AD.

ACKNOWLEDGMENTS

This work was supported in part by the National Natural Science Foundation of China under Grant 62376150 and 62303295, in part by the Shandong Provincial Natural Science Foundation, China under Grant ZR2015FL004. We also express our gratitude to the Department of Neurology, Xuanwu Hospital of Capital Medical University.

CONFLICT OF INTEREST STATEMENT

The authors have no conflicts to disclose.

DATA AVAILABILITY STATEMENT

ADNI datasets can be downloaded from the ADNI website. Xuanwu datasets are available from the corresponding author on reasonable request.

REFERENCES

1. Gaugler J, James B, Johnson T, Marin A, Weuve J, Alzheimer's A. 2019 Alzheimer's disease facts and figures. *Alzheimers Dement*. 2019;15(3):321-387. doi: https://doi.org/10.1016/j.jalz.2019.01.010
2. Plassard AJ, Bao S, McHugo M, et al. Automated, open-source segmentation of the hippocampus and amygdala with the open Vanderbilt archive of the temporal lobe. *Magn Reson Imaging*. 2021;81:17-23. doi: https://doi.org/10.1016/j.mri.2021.04.011
3. Wu J, Dong Q, Gui J, et al. Predicting brain amyloid using multivariate morphometry statistics, sparse coding, and correntropy: validation in 1,101 individuals from the ADNI and OASIS databases. *Front Neurosci*. 2021;15: 669595. doi: https://doi.org/10.3389/fnins.2021.669595
4. Zhao K, Ding Y, Han Y, et al. Independent and reproducible hippocampal radiomic biomarkers for multisite Alzheimer's disease: diagnosis, longitudinal progress and biological basis. *Sci Bull*. 2020;65(13):1103-1113. doi: https://doi.org/10.1016/j.scib.2020.04.003
5. Wang G, Dong Q, Wu J, et al. Developing univariate neurodegeneration biomarkers with low-rank and sparse subspace decomposition. *Med Image Anal*. 2021;67:101877. doi: https://doi.org/10.1016/j.media.2020.101877
6. Collin SHP, Milivojevic B, Doeller CF. Memory hierarchies map onto the hippocampal long axis in humans. *Nat Neurosci*. 2015;18(11):1562-1564. doi: https://doi.org/10.1038/nn.4138
7. Pan Y, Liu J, Tian X, Lan W, Guo R. Hippocampal segmentation in brain MRI images using machine learning methods: a survey. *Chin J Electron*. 2021;30(5):793-814. doi: https://doi.org/10.1049/cje.2021.06.002
8. Wang W, Zhang X, Ma Y, Cui H, Xia R, Zhang Y. A robust discriminative multi-atlas label fusion method for hippocampus segmentation from MR image. *Comput Meth Programs Biomed*. 2021;208:106197. doi: https://doi.org/10.1016/j.cmpb.2021.106197
9. Nouri M, Baleghi Y. An active contour model reinforced by convolutional neural network and texture description. *Neurocomputing*. 2023;528:125-135. doi: https://doi.org/10.1016/j.neucom.2023.01.047
10. Cao L, Li L, Zheng J, et al. Multi-task neural networks for joint hippocampus segmentation and clinical score regression. *Multimed Tools Appl*. 2018;77(22):29669-29686. doi: https://doi.org/10.1007/s11042-017-5581-1
11. Isensee F, Petersen J, Klein A, et al. nnU-Net: self-adapting framework for U-Net-based medical image segmentation. *arXiv preprint arXiv: 180910486*. 2018.
12. Wang L, Chen R, Wang S, Zeng N, Huang X, Liu C. Nested dilation network (NDN) for multi-task medical image segmentation. *IEEE Access*. 2019;7:44676-44685. doi: https://doi.org/10.1109/ACCESS.2019.2908386
13. Huang X, Wang J, Li Z. 3D carotid artery segmentation using shape-constrained active contours. *Comput Biol Med*. 2023;153:106530. doi: https://doi.org/10.1016/j.compbiomed.2022.106530
14. Calisto MB, Lai-Yuen SK. EMONAS-Net: efficient multiobjective neural architecture search using surrogate-assisted evolutionary algorithm for 3D medical image segmentation. *Artif Intell Med*. 2021;119:102154. doi: https://doi.org/10.1016/j.artmed.2021.102154
15. Jaidilert S, Farooque G. Crack detection and images inpainting method for Thai mural painting images. Paper presented at: 2018 *IEEE 3rd International Conference on Image, Vision and Computing (ICIVC)*. 2018.
16. Chen Y, Lu D, Courbebaisse G. A parallel image registration algorithm based on a lattice Boltzmann model. *Information*. 2020;11(1):1. doi: https://doi.org/10.3390/info11010001
17. Liu Y, Yan Z. A combined deep-learning and lattice Boltzmann model for segmentation of the hippocampus in MRI. *Sensors-Basel*. 2020;20(13):3628. doi: https://doi.org/10.3390/s20133628
18. Patenaude B, Smith SM, Kennedy DN, Jenkinson M. A Bayesian model of shape and appearance for subcortical brain segmentation. *Neuroimage*. 2011;56(3):907-922. doi: https://doi.org/10.1016/j.neuroimage.2011.02.046
19. Li K, Fan L, Cui Y, et al. The human mediodorsal thalamus: organization, connectivity, and function. *Neuroimage*. 2022;249:118876. doi: https://doi.org/10.1016/j.neuroimage.2022.118876
20. Li C, Kao CY, Gore JC, Ding Z. Implicit active contours driven by local binary fitting energy. Paper presented at: *2007 IEEE Conference on Computer Vision and Pattern Recognition (CVPR)*. 2007.
21. Song Y, Peng G. Improving the convergence of local binary fitting energy for image segmentation. Paper presented at: *10th International Conference on Graphics and Image Processing (ICGIP)*. 2018.
22. Li C, Xu C, Gui C, Fox MD. Distance regularized level set evolution and its application to image segmentation. *IEEE T Image Process*. 2010;19(12):3243-3254. doi: https://doi.org/10.1109/TIP.2010.2069690
23. Lemasson B, Christen T, Serduc R, et al. Evaluation of the relationship between MR estimates of blood oxygen saturation and hypoxia: effect of an antiangiogenic treatment on a gliosarcoma model. *Radiology*. 2012;265(3):743-752. doi: https://doi.org/10.1148/radiol.12112621
24. Zheng Q, Liu B, Gao Y, et al. HGM-cNet: integrating hippocampal gray matter probability map into a cascaded deep learning framework improves hippocampus segme ntation. *Eur*

J Radiol. 2023;162:110771. doi: https://doi.org/10.1016/j.ejrad.2023.110771
25. Thyreau B, Sato K, Fukuda H, Taki Y. Segmentation of the hippocampus by transferring algorithmic knowledge for large cohort processing. *Med Image Anal*. 2018;43:214-228. doi: https://doi.org/10.1016/j.media.2017.11.004
26. Kirillov A, Mintun E, Ravi N, et al. Segment anything. *arXiv preprint arXiv: 230402643*. 2023.
27. Tran M, Ly L, Hua BS, Le N. SS-3DCapsNet: Self-supervised 3D capsule networks for medical segmentation on less labeled data. Paper presented at: *IEEE 19th International Symposium on Biomedical Imaging (ISBI)*. 2022.
28. Bala SA, Kant S. Dense dilated inception network for medical image segmentation. *Int J Adv Comput Sc*. 2020;11(11):785-793. doi: https://doi.org/10.14569/ijacsa.2020.0111195
29. Folle L, Vesal S, Ravikumar N, Maier A. Dilated deeply supervised networks for hippocampus segmentation in MRI. *arXiv preprint arXiv: 190309097*. 2019.
30. Wang J, Wang P, Jiang Y, et al. Hippocampus-based dynamic functional connectivity mapping in the early stages of Alzheimer's disease. *J Alzheimers Dis*. 2022;85(4):1795-1806. doi: https://doi.org/10.3233/JAD-215239
31. Lyman C, Lee D, Ferrari H, et al. MRI-based thalamic volumetry in multiple sclerosis using FSL-FIRST: systematic assessment of common error modes. *J Neuroimaging*. 2022;32(2):245-252. doi: https://doi.org/10.1111/jon.12947
32. Li W, Fan L, Shi W, et al. Brainnetome atlas of preadolescent children based on anatomical connectivity profiles. *Cereb Cortex*. 2023;33(9):5264-5275. doi: https://doi.org/10.1093/cercor/bhac415
33. Stonnington CM, Wu J, Zhang J, et al. Improved prediction of imminent progression to clinically significant memory decline using surface multivariate morphometry statistics and sparse coding. *J Alzheimers Dis*. 2021;81(1):209-220. doi: https://doi.org/10.3233/JAD-200821
34. Feng F, Wang P, Zhao K, et al. Radiomic features of hippocampal subregions in Alzheimer's disease and amnestic mild cognitive impairment. *Front Aging Neurosci*. 2018;10:290. doi: https://doi.org/10.3389/fnagi.2018.00290

SUPPORTING INFORMATION

Additional supporting information can be found online in the Supporting Information section at the end of this article.

How to cite this article: Liu Y, Wang M, Yu X, Han Y, Jiang J, Yan Z. An effective and robust lattice Boltzmann model guided by atlas for hippocampal subregions segmentation. *Med Phys*. 2024;1-16. https://doi.org/10.1002/mp.16984